Optical and Near-Infrared Structural Properties of Cluster Galaxies at $z \sim 0.3^1$

F. La Barbera

Physics Department, Università Federico II, Napoli, Italy

labarber@na.astro.it

G. Busarello, P. Merluzzi and M. Massarotti

Osservatorio Astronomico di Capodimonte, Napoli, Italy

gianni@na.astro.it

merluzzi@na.astro.it

michele@na.astro.it

and

M. Capaccioli

Physics Department, Università Federico II, Napoli, Italy
Osservatorio Astronomico di Capodimonte, Napoli, Italy

capaccioli@na.astro.it

ABSTRACT

Structural parameters (half-light radius r_e , mean effective surface brightness $\langle \mu \rangle_e$, and Sersic index n, parameterizing the light profile shape) are derived for a sample of galaxies in the rich cluster AC 118 at z=0.31: so far the largest (N=93) sample of galaxies at intermediate-redshift with structural parameters measured in the near-infrared. The parameters are obtained in two optical wavebands (V and R) and in the K-band, corresponding approximately to B, V and H rest-frame.

The distributions of r_e at z=0.31 match those for the Coma cluster (i.e. for the local universe) both in the optical and in the NIR. The K-band distribution is of particular interest, since the NIR light mimics the mass distribution of galaxies. The similarity of the distributions for the two clusters (AC 118 and

Coma) proves that the galaxies at the bright end of the luminosity function did not significantly change their sizes since $z \sim 0.3$ to the present epoch.

The ratio of the optical to the NIR half-light radius shows a marked trend with the shape of the light profile (Sersic index n). In galaxies with $n \gtrsim 4$ (typical bright ellipticals) $r_{e,NIR} \sim 0.6 r_{e,opt}$, while the average ratio is 0.8 for galaxies with lower n (typical disk systems). Moreover, the NIR Sersic index is systematically larger than in the optical for $n \lesssim 4$. These results, translated into optical and optical-NIR color gradients, imply that the optical color gradients at $z \sim 0.3$ are similar to those of nearby galaxies. The optical-NIR color gradients are in the average larger, ranging from -0.73 mag/dex for $n \lesssim 4$ to -0.35 mag/dex for $n \gtrsim 4$.

Models with 'pure age' or 'pure metallicity' gradients are unable to reconcile our color gradients estimates with observations at $z \sim 0$, but we argue that the combined effects of age and metallicity might explain consistently the observed data: passive evolution (plus the possible effect of dust absorption) may account for the differences between the optical and NIR structural properties.

The lack of any major change in $r_{e,NIR}$ since $z \sim 0.3$ suggests that merging involving bright galaxies did not play a significant role in the last ~ 4.4 Gyr $(\Omega_M=0.3, \Omega_{\Lambda}=0, H_0=50 \text{ km s}^{-1}\text{Mpc}^{-1})$.

The results of the present paper will be applied to the study of the scaling laws in subsequent works.

Subject headings: galaxies: clusters: individual: AC 118 – galaxies: evolution – galaxies: fundamental parameters (effective radius, surface brightness, Sersic index) – galaxies: photometry

1. Introduction

Our knowledge on the evolution of galaxies comes from the study of the properties of families of galaxies at different redshifts. Observable quantities like magnitudes, colors, structural parameters, velocity dispersions and line strengths are combined into well-established relations like, for instance, the color-magnitude relation (e.g. Bower, Lucey, & Ellis 1992; Kodama et al. 1998), the Mg- σ relation (Ziegler & Bender 1997), the fundamental plane (Dressler et al. 1987; Djorgovski & Davies 1987; Jørgensen, Franx, & Kjærgaard 1996) and

¹Based on observations collected at European Southern Observatory (ESO n. 62.O-0369, 63.O-0257, 64.O-0236) and on data from the STScI Science Archive

its projection in the $r_e - \langle \mu \rangle_e$ plane, that is the Kormendy relation (Kormendy 1977; Capaccioli, Caon, D'Onofrio 1992; Ziegler et al. 1999). These relations can now be studied over a significant fraction of the age of the universe. Studies of the properties of early-type galaxies in rich clusters lead to a large amount of observational evidence in favor of the passive evolution scenario, in which an early (z > 2) and short (\sim 1 Gyr) burst of star formation is followed by a long period where the aging of stellar populations drives the observed properties of galaxies through intermediate redshifts until the present epoch (Kodama & Arimoto 1997; Stanford, Eisenhardt, & Dickinson 1998; Jørgensen et al. 1999; Kelson et al. 2000a, and references therein). On the other side, the alternative scenario of the hierarchical merging seems also consistent with most of the existing data (e.g. Kauffmann & Charlot 1998), indicating either that the present observational evidence is not sufficient to discriminate between the two pictures or that galaxy evolution is driven by both mechanisms.

The half-light radius and the mean surface brightness of a galaxy measure the size and the density of the luminous matter. These quantities are related both to the gravitational potential of the galaxy and to the properties of the stellar populations. The relations existing between the structural parameters of galaxies have been recently studied at intermediate redshifts, both in the form of r_e vs. $\langle \mu \rangle_e$ (Ziegler et al. 1999, and references therein) and as luminosity-size relation (Schade et al. 1996; Simard et al. 1999). Schade et al. (1996) found that disks at z > 0.5 are in the average ~ 1.5 mag brighter than in local galaxies. This was contrasted by the results of Simard et al. (1999) who found no luminosity evolution in disks up to $z \sim 0.9$. Ziegler et al. (1999) found that the Kormendy relation of cluster galaxies at z = 0.4 and z = 0.55 is consistent with the passive evolution scenario. The Kormendy relation has also proven to be a powerful tool to test the expansion of the universe by the measurement of the cosmological dimming (i.e. for the Tolman test). Lubin & Sandage (2001) studied the Kormendy relation up to z = 0.92, finding that the data are consistent with the cosmic expansion together with passive evolution. Finally, the structural parameters enter the fundamental plane of early-type galaxies, of which the Kormendy relation is a twodimensional projection. Due to its very small scatter, the fundamental plane is a powerful tool to study the evolution of the M/L ratio of galaxies belonging to distant clusters. The recent determinations of the fundamental plane at intermediate redshifts constrain the epoch of star formation in early-type galaxies at large redshifts (z >2 for Ω_M =0.3 or z >5 for Ω_M =1 and $\Omega_{\Lambda} = 0$; see van Dokkum & Franx 1996; Jørgensen et al. 1999; Kelson et al. 2000a). However, these studies have to face with the problem of the progenitor bias, i.e. with our ignorance of the relationship between local galaxies and their high redshift counterparts (see van Dokkum & Franx 2001 for a thorough discussion).

A clue for the interpretation and for the applications of the scaling laws is the dependence of the structural parameters on wavelength. The basic distinction between optical and

NIR is that the optical wavebands are very sensitive to the effects of metallicity (through line-blanketing) and to the content of younger populations (dust absorption included), while the NIR wavebands are dominated by the old, more quiescent, stellar populations and are virtually unaffected by dust absorption. For these reasons the NIR is the best tracer of the mass distribution inside a galaxy. Local galaxies are smaller at NIR wavebands than in the visible, with a similar, though weaker, trend also within the optical wavelength range (Scodeggio et al. 1998; Pahre, de Carvalho, & Djorgovski 1998). This behavior is confirmed by the relatively large optical-NIR color gradients measured in early-type galaxies, the optical-optical gradients being usually much smaller, except when the U-band is involved (Peletier et al. 1990a; Peletier, Valentijn, & Jameson 1990b; Hinkley & Im 2001; Nelson et al. 2001). Small optical color gradients were recently measured in distant (up to $z \sim 1$) cluster early-type galaxies by Saglia et al. (2000) and by Tamura et al. (2000). These authors concluded that metallicity is the primary factor driving the color gradients.

The derivation of the structural parameters at intermediate redshifts is affected by the problem of the small angular size of the galaxies, whose half-light radii are typically less than 1 arcsec. For this reason many works were based on imaging taken with the HST. It has been demonstrated, however, that reliable structural parameters can be derived from ground-based photometry as well, on high resolution (< 0.1''/pxl) and exceptional seeing (< 0.4'') conditions, provided that the properties of the PSF are carefully taken into account (Schade et al. 1996; Jørgensen et al. 1999).

In this paper we obtain the first multi-band large set of structural parameters for galaxies at an intermediate redshift (z=0.31). The data are derived from ground-based (ESO-NTT) photometry in two optical (V and R) and one NIR (K) wavebands. The derived values for the structural parameters will be published in a forthcoming paper addressed to the study of galaxy evolution by means of the scaling laws (Busarello et al. 2001a, in preparation).

The paper is organized as follows. The sample and the data used in this study are presented in § 2. The derivation of the structural parameters is outlined in § 3. The structural parameters from HST imaging are derived in § 4, where the results from Sersic models and bulge-disk decomposition are compared. In § 5 we use HST photometry for a subset of galaxies to verify the reliability of ground-based structural parameters. The structural parameters are presented in § 6, where we make a comparison between optical and NIR properties at $z \sim 0.3$ and with the values at $z \sim 0$. In § 7 we analyze the optical and NIR structure of galaxies in terms of internal color gradients. The results are discussed in § 8.

2. Description of the Sample

AC 118 (Abell 2744) is a rich ('Coma-like') galaxy cluster at redshift z = 0.31 that was studied by several authors in relation to its galaxy population, X-ray and radio properties and gravitational lensing (Barger et al. 1996; Couch et al. 1998; Stanford et al. 1998; Williams, Navarro, & Bartelmann 1999; Wu, Xue, & Fang 1999; Allen 2000; Govoni et al. 2001).

New photometric data and medium resolution spectroscopy has been collected during three observing runs (October 1998 - September 2000) at the ESO New Technology Telescope. The data of interest for the present work are the imaging in the V and R wavebands obtained with the EMMI instrument and the imaging in the K waveband obtained with SOFI. The photometry is complemented with HST archive data consisting of a single pointing on the cluster center. The relevant information on the data is given in Table 1. The reduction of the K-band image is described in Andreon (2001), while the reduction of the NTT optical data will be presented elsewhere (Busarello et al. 2002b, in preparation). The HST data were retrieved from the STScI Archive and reduced following the steps described in Couch et al. (1998). The NTT photometry was used to calibrate the HST imaging into the Johnson R-band as outlined in Appendix A.

The samples used in the present study consist in: A) 50 galaxies in the HST field; B) 37 galaxies in the HST field in common with the ground-based R-band sample; C) 58 galaxies in common in the V- and R-band; D) 93 galaxies in common in the R- and K-band.

Samples C and D are the results of two selection steps. The first selection was based on photometric redshifts (Massarotti, Iovino, & Buzzoni 2001), as derived from the above photometry plus I- and U-band (new NTT data and NTT archive data respectively). The reliability of the photometric redshifts was verified on 75 galaxies with available spectra (Merluzzi et al. 2002, in preparation). Morphology is not a selection criterion in this study, since a morphological classification is not possible from our data. The photometric redshifts algorithm flags the galaxies according to whether their colors are consistent with early-or late-type template spectra. We did not use this classification as a selection criterion, and retained in the samples all the galaxies with the correct photometric redshift. We remark, however, that only 7 galaxies out of 93 in sample D are 'late-type' according to their photometric properties (from U to K). The second selection step is based on the reliability of the measurement of the structural parameters and is the result of the analysis presented in § 3.3. This lead to include in the sample the galaxies brighter than R=21 and V=20.5, and to exclude objects with an estimated r_e smaller than 0.15 arcsec.

Samples A and B were selected in order to obtain 1) reliable structural parameters in the NTT R-band and 2) the largest number of galaxies in the HST field with the same

range of sizes and luminosities of the ground-based samples. This lead to include galaxies brighter than R=21 and to exclude objects with r_e smaller than 0.15 arcsec both in the NTT and in the HST image. A further (a posteriori) selection was done for all the samples on the basis of the results of the fitting: objects with very large uncertainties (>100%) were not considered in the analysis. This however lead to exclude only 2% of the objects.

Morphological classification from HST imaging by Couch et al. (1998) is available for 21 out of 93 galaxies in sample D (17 out of 58 in sample C). Out of these, 6 (6) are classified as ellipticals, 10 (7) as S0, and 5 (4) as spirals. These numbers reflect the overall distribution of morphological types in AC 118, which is dominated by early-type (mainly S0) galaxies (Couch et al. 1998). The question of morphological types will be resumed in the conclusions. The relevant information on the samples is summarized in Table 2.

3. Derivation of the structural parameters

Since the typical galaxy sizes at $z \sim 0.3$ are smaller than $\sim 1''$, it is crucial to take into account the effects of the Point Spread Function (PSF) when deriving structural parameters from ground-based data. This means that a proper model for the galaxy surface brightness (SB) has to be convolved with the PSF and fitted to the observed SB. This is usually performed: 1) by one-dimensional fitting algorithms (e.g. Saglia et al. 1997) or 2) by two-dimensional methods (van Dokkum & Franx 1996; Simard et al. 1999). In case 1) the integrated light curve or the SB profile are derived by an elliptical fit to the galaxy isophotes and then fitted with the adopted model. In the two-dimensional approach, a direct fit of the galaxy SB is performed. Advantages and drawbacks of both methods have been largely discussed in previous works (see Kelson et al. 2000b, and references therein). In the present study we adopt the two-dimensional fitting approach for two reasons: 1) many galaxies in AC 118 belong to overlapping systems, and only the 2D approach can deal properly with these cases; 2) isophotal fitting of the ground-based images should be performed on a very small number of pixels, resulting in poorly constrained isophotes.

The SB of distant galaxies is well described by two-dimensional models with constant ellipticity and position angle. In this study, we use two kinds of models: the Sersic model (Sersic 1968) and the $(r^{1/4}-)$ bulge + disk (B+D) model. Since the B+D decomposition requires high resolution and signal to noise ratios (see Ratnatunga, Griffiths, & Ostrander 1999), this model is applied only to the HST data. Ground-based structural parameters are derived by fitting the Sersic models. The models used for the PSF of the NTT and HST images are presented in § 3.1 while the fitting algorithm and the galaxy models are described in § 3.2. The limits of applicability of the fitting algorithm are set in § 3.3.

3.1. The Point Spread Function

To model the PSF of the HST image, we used the Tiny Tim 5.0 software package (Krist 1999). Since the PSF depends on the position on the field, different models were created for each galaxy at the corresponding chip location. Effects of PSF under-sampling and broadening from image jittering are smaller than few percents of r_e for the typical sizes of galaxies at this redshift and therefore these were ignored (see Kelson et al. 2000b).

To model the PSF of the NTT images we proceeded as follows. Stars in the cluster field were selected by the stellar index parameter SG of S-Extractor (Bertin & Arnouts 1996) and from the aperture magnitude. To minimize star – galaxy classification errors, we considered only objects with $SG \geq 0.99$. We selected sources with $K \leq 18$ mag in the SOFI field and $R \leq 21$ mag in the region not covered from the infrared imaging. Such criteria allowed to obtain a sufficient S/N to model the PSF. The reliability of the selection is also supported by the photometric redshift algorithm: the colors of the candidate stars do not match galaxy template spectra at any redshift.

The PSF of the NTT images is well described by a sum of two Gaussians convolved with the pixel function (see appendix B for details). The model has nine relevant parameters: the center coordinates, the central intensity, the Full Width at Half Maximum (FWHM) of the two Gaussians in the two perpendicular directions, the ratio of the central intensities, and the local value of the background. The fits were performed by a χ^2 minimizing algorithm based on the Levenberg-Marquardt method (Press et al. 1986). Typically, the residuals from the fitting are smaller than 5%. The uncertainties on fitting parameters were estimated by numerical simulations on models with Gaussian noise. For each pixel, the standard deviation of the noise was computed by the distribution of the fit residuals in the adjacent pixels². Figure 1 shows the values of the PSF parameters in the V-, R- and K-band as a function of the distance to the image centers. In general the PSF tends to become broader as this distance increases. The effect is very weak in the K-band image, while significant variations are found in the optical images. The trends of the parameters were modeled with empirical analytic curves, that were then used to obtain the PSF model relative to each galaxy position.

²This allows to take into account empirically the various sources of uncertainties: flat-field accuracy, photon and read-out noise, deviations from the fit model, etc.

3.2. Modeling of the brightness distribution

Galaxy images were fitted by the following model:

$$M(BG, \{p_k\}) = BG + B(\{p_k\}) \circ S$$
 , (1)

where B is the galaxy brightness distribution, that is described by a set of parameters $\{p_k\}$, S is the PSF model, BG is the value of the local background, and the symbol \circ denotes the convolution. For the Sersic models, the parameters $\{p_k\}$ are: the effective major semi-axis R_e , the central surface brightness I_0 , the Sersic index n, the axial ratio b/a, the position angle PA, the coordinates of the photometric center and the local value of the background. In the case of the B+D decomposition, the parameters that enter the fit are those of two Sersic models with n=4 and n=1 for the bulge and the disk respectively. The fit parameters are used to derive the total magnitude m_T (e.g. Saglia et al. 2000), r_e and $\langle \mu \rangle_e$. For Sersic models, r_e is computed as the equivalent radius of the ellipse that encloses half of the total galaxy light, i.e. $r_e = \sqrt{b/a} \cdot R_e$. For the B+D decomposition, r_e is calculated from the growth curve of circular aperture magnitudes. In both cases, we have $\langle \mu \rangle_e = 2.5 \log(2\pi) + 5 \log(r_e) + m_T$. For the Sersic models we found that both methods of computing r_e agree within 2%. Therefore, the difference of the two definitions can be ignored in the following analysis.

The parameters $\{p_k\}$ and BG were derived by a least squares fit, by minimizing the function

$$\chi^{2}(BG, \{p_{k}\}) = f(\{p_{k}\}) \cdot \left[\sum_{j} (I_{j} - M_{j}(BG, \{p_{k}\}))^{2} \right] , \qquad (2)$$

where I_j is the observed brightness distribution, j is an index running on image pixels and f is a penalty function introduced to avoid 'not allowed' regions of the parameter space (i.e. unrealistic values that can be found on local minima of χ^2). The χ^2 minimization was performed by the Levenberg-Marquardt algorithm. The convolution with the PSF was computed straightly in the real domain in order to avoid high frequencies problems when convolving galaxy models by the Fast Fourier Transform. Bad pixels, degraded regions and pixels contaminated by background objects, were excluded from summation in equation 2. To this aim, a masking image was created interactively for each galaxy. Overlapping objects were fitted simultaneously.

Uncertainties on structural parameters are usually estimated either from the formal errors on fitting results or by numerical simulations. The formal uncertainties are derived by the topology of the χ^2 function near to the solution and therefore they do not take into account the various sources of errors on the estimated parameters (e.g. Smith et al. 1997). Numerical simulations give more reliable uncertainties but they depend on the adopted

galaxy model and are much more expensive in terms of computation time. As a compromise between accuracy and amount of computation time, we used a first order approximation: the uncertainties on the fit parameters were estimated from the derivatives of the χ^2 function taking into account the noise in the galaxy image and the uncertainties on the PSF parameters. Details are given in Appendix C.

3.3. Simulations

To test the performance of the fitting procedure and to set the limits to its applicability, we created two sets of simulations based on Sersic $r^{1/n}$ models convolved with the NTT R-band PSF and with the typical noise of ground-based data. To take into account the uncertainties on the PSF, all the simulations were generated with the same PSF but the fits were performed with different PSF models whose parameters were generated in agreement with the corresponding uncertainties (see § 3.1).

The first set of simulations consist in $r^{1/4}$ galaxies spanning the full magnitude range in the R-band (19 mag $\leq m_T \leq 23$ mag). Two values of r_e were considered: $r_e = 0.3''$ and $r_e = 0.6''$, that correspond to the sizes of a small and a typical galaxy in a cluster at $z \sim 0.3$ (e.g. Kelson et al. 2000a). In Figure 2 we give the results of the simulations in terms of differences between the input model parameters and the output from the fitting procedure. The quantities shown are r_e , the axis ratio b/a (both given as logarithms), m_T , $\langle \mu \rangle_e$, n, and the 'fundamental plane parameter', $FP = \log r_e - 0.3 \times \langle \mu \rangle_e$, that is the combination of the structural parameters entering the fundamental plane. It can be seen that the scatter of the fit parameters around the 'true' values is relatively small for $m_T < 22$ where it amounts at most to 25% in r_e , 0.5 mag in $\langle \mu \rangle_e$, 0.15 mag in m_T , 15% in FP and 10% in b/a. The scatter of n is higher, and varies from $\Delta n \sim 1$ at $m_T = 19$ mag up to $\Delta n \sim 3$ at $m_T = 22$ mag. Objects fainter than $m_T = 22$ mag are affected by larger and systematic differences between input and computed parameters.

The second set of simulations was created in order to test the fitting algorithm with respect to the galaxy size. To this aim, a wide range of values of r_e was explored ($r_e = 0.05''$ to $r_e = 3''$) for three Sersic models with n = 1, 4, 7 respectively. For each value of r_e , a suitable value of $\langle \mu \rangle_e$ was derived from the Kormendy relation, whose slope and the zero point were calibrated a posteriori from the present sample. In Figure 3, we show the comparison between true and estimated parameters. An inspection of Figure 3 shows that the parameters are recovered with a relatively small scatter (see above) and without systematic errors for $r_e > 0.15''$ (log $r_e > -0.8$) for the whole range of n values. The shape of light profile is subject to a small systematic error ($\Delta n \sim 1$) for n = 7 below $r_e \sim 0.5''$ (log $r_e \sim -0.3$). We

also notice that the scatter increases for large n values, due to the effect of the uncertainties on the PSF for galaxies with more concentrated profiles.

The above results were used to derive the selection of the samples in this study. All the samples include the galaxies with $r_e > 0.15''$ in each band; in the R-band only galaxies with R <21 mag were included as a conservative limit; in the V-band a more restrictive selection in magnitude (V <20.5 mag) was necessary due to the lower S/N, while no further restriction was needed for the K-band photometry.

4. HST structural parameters

Structural parameters were derived for N=50 galaxies in the HST image (sample A of Table 2), 42 of these objects are cluster members according to the photometric redshifts. Galaxies were fitted by both Sersic and B+D models, and a flag F was assigned to each galaxy for the different cases that were encountered during the fitting. For N=5 galaxies, both models gave small fitting residuals, but the B+D decomposition produced meaningless values of the structural parameters for the bulge or for the disk component (e.g. $r_e < 0.02''$). For such galaxies a possible second physical component is too weak or too small to be detected. However, except for one object that was excluded from the analysis, acceptable global parameters $(r_e \text{ and } \langle \mu \rangle_e)$ were obtained from the B+D fit so that such galaxies were retained in the sample and were flagged with F = -1. For N = 24 objects, both Sersic and B+D models gave small fitting residuals and acceptable estimates of the parameters. They were flagged with F=0. F=1 was used to indicate N=14 galaxies for which residuals from the Sersic model shown evidence for a second component that was properly described with the B+D decomposition. The flags F=0 and F=1 were assigned by visual inspection of the galaxy fits as illustrated in Figure 4. Finally, N=7 galaxies, of which some objects with very distorted morphology and some BCGs with very large residuals (> 50%), were flagged with F = -2 and excluded from the present analysis. Fitting models suitable for such objects will be discussed in a forthcoming work.

In Figure 5, we compare the structural parameters r_e , $\langle \mu \rangle_e$, m_T and FP obtained by different models. Table 3 shows the medians and the standard deviations of the differences in fitting parameters, and the relative bootstrap confidence intervals. By weighting each point in Figure 5 with the fitting uncertainties (§ 3.2), we did not find significant variations of the estimates given in Table 3. This also holds for the other comparisons of structural parameters in the present work (see § 4 and § 5).

It is clear from Table 3 and from Figure 5 that the mean differences of the parameters

have no significant biases, also when galaxies with different flag F are considered. On the other side, the scatter in the structural parameters depends on the F value: as expected, minimum values are obtained for F=0 when B+D and Sersic models give an equivalent description of the galaxy image. The scatter varies from 35% to 50% for r_e , from ~ 0.8 mag to 1.3 mag for $\langle \mu \rangle_e$, and from ~ 0.25 mag to ~ 0.43 mag for m_T . One important fact is the robustness of the FP parameter against the adopted fitting method: due to the correlation between the errors in r_e and in $\langle \mu \rangle_e$ (Hamabe & Kormendy 1987; Jørgensen, Franx,& Kjærgaard 1995), its scatter varies from $\sim 7\%$ for F=0 to $\sim 14\%$ for F=-1. The previous results are fully consistent with the findings of Kelson et al. (2000a), although they find a smaller dispersion ($\sim 3\%$) between the FP parameters derived by different fitting methods. The results shown in Figure 5 and Table 3 give a measure of the intrinsic uncertainties on the structural parameters of the galaxies in the present sample and will be used as a reference in the following sections.

5. Comparison of HST and NTT surface photometry

The 2D fits for a representative subsample of galaxies in the HST and NTT R-band images are shown in Figure 6. Although the residuals from the fit are more evident in the HST images due to the higher resolution and to the higher S/N, both HST and ground-based images can be suitably fitted with the $r^{1/n}$ models, also when overlapping objects are considered.

To test the reliability of the ground-based structural parameters, we compared the estimates obtained by fitting Sersic models to the HST and the NTT images of galaxies in the sample B of Table 2. Since both filters cover approximately the same spectral range (rest-frame V-band), we can rule out any difference between the two datasets due to a possible waveband dependence of the structural parameters. The structural parameters are compared in Figure 7, where we plot the same quantities as in Figure 5. The medians and the standard deviations of the differences in $\log r_e$, $\langle \mu \rangle_e$, m_T and FP are given in Table 4. Table 4 and Figure 7 prove that the mean differences of the parameters have no significant biases. The scatter between the two sets of measurements is relatively small: it amounts to $\sim 38\%$ for r_e , ~ 0.7 mag for $\langle \mu \rangle_e$, ~ 0.3 mag for m_T and $\sim 13\%$ for the FP parameter. It is worth to stress again that the FP parameter has significantly smaller dispersion with respect to the other quantities. The comparison with the results of the previous sections proves that the differences in the parameters derived from HST and from NTT photometry are of the same order of those found when applying different fitting methods to the HST image. In other words, the difference between the structural parameters derived from HST

and from NTT data is consistent with the precision with which these quantities can be measured (see Kelson et al. 2000a; Jørgensen et al. 1999). We thus conclude that reliable structural parameters can be still derived for typical sizes and luminosities of cluster galaxies at redshift $z \sim 0.3$ by using ground-based data taken in ordinary observing conditions (i.e. seeing $\sim 1''$ and pixel scale $\sim 0.28''/\text{pxl}$).

6. Optical and Near-Infrared Structural Parameters

6.1. Structure of Galaxies at $z \sim 0.3$

The V- and R-band structural parameters for N=58 galaxies (sample C of Table 2) are compared in Figure 8 and Table 5. To allow a direct comparison, $\langle \mu \rangle_e$ and m_T of V-band galaxies were corrected with the observed V-R colors (Busarello et al. 2002b, in preparation). V- and R-band parameters show no significant systematic differences and the scatter between the two sets of data is of the same order as those found in the preceding sections, i.e. equal to the typical uncertainty of structural parameter measurements. The mean ratio $r_{e,R}/r_{e,V} \sim 0.97^{1.00}_{0.91}$ is consistent with that found in local early-type galaxies ($r_{e,I}/r_{e,V} \sim 0.91$, Scodeggio 2001; see also Scodeggio et al. 1998). We defer further considerations to § 7, where the results will be discussed in terms of color gradients. Our R-band structural parameters can be directly compared to those derived at z=0.33 by Kelson et al. (2000b) in the same wavelength range. The full consistency of the two data sets is apparent from Figure 9 (upper panel) where the distributions of half-light radii are compared (the surface brightness is not shown for brevity reasons).

The R- and K-band structural parameters for the 93 galaxies in sample D (Table 2) are compared in Figure 10 and Table 6. NIR r_e and $\langle \mu \rangle_e$ are significantly smaller than the relative optical parameters, while the n values are systematically higher. On the average, such differences amount to -0.125 in $\log r_e$, to -0.5 mag in $\langle \mu \rangle_e$ and to +0.5 in n. A deeper inspection reveals the existence of two distinct subsamples which are separated by the value of the Sersic parameter. For low n values (n < 4), the differences of K- to R-band effective radii amount to -0.09 in $\log r_e$, and the differences in the Sersic index are higher ($\Delta n \sim 1$ instead of 0.5). On the other side, for n > 4 the Sersic indices are nearly the same in the two wavebands ($\Delta n \sim 0$) while the K-band half-light radii are much smaller than in the optical (-0.2 dex). The confidence limits in Table 6 show that the separation into the two classes is highly significant. According to the Kolmogorov-Smirnov test, the probability that the two samples come from the same distribution is less than 2% for both Δn and $\Delta \log r_e$.

The results of the previous sections make us confident that the systematic differences

found between the structural parameters are real and do not originate from biases induced by the fitting method. No other measurements of K-band (rest-frame H) structural parameters are available at $z \sim 0.3$ so that no direct comparison is possible. Again we defer further considerations to § 7.

6.2. Comparison with Local Galaxies

To make a comparison with the structural properties of nearby galaxies, we made use of the sample of 70 galaxies belonging of the Coma Cluster from the compilation by Pahre (1999). The distribution of the V-band r_e from Pahre (1999) is shown in Figure 9 (notice that our R-band corresponds to the rest-frame V-band). The radii of Pahre (1999) were scaled to z = 0.31 by adopting $\Omega_M = 0.31$, $\Omega_{\Lambda} = 0$ (different cosmologies do not significantly alter the result).

The distributions of NIR r_e are also compared in Figure 9 (the radii of Pahre 1999 were scaled as above). It is worth noticing that, although our rest-frame waveband is different from the K-band in Pahre (1999), the two wavebands actually probe the same stellar populations, so that the direct comparison has an immediate physical interpretation. The medians of the distributions in the NIR are $-0.22^{-0.18}_{-0.25}$ and $-0.22^{-0.18}_{-0.25}$ for Coma and AC 118 respectively, while the corresponding values in the optical are $-0.12^{-0.08}_{-0.15}$ and $-0.08^{-0.04}_{-0.12}$. We thus conclude that the median of the half-light radii at $z \sim 0.3$ is fully consistent with the median at $z \sim 0$ both in the optical and in the NIR.

This result indicates that the sizes of bright galaxies did not substantially change since $z \sim 0.3$ to the present epoch. Since the NIR probes directly the mass distribution inside galaxies, and assuming that changes in mass produce corresponding changes in size, we argue that during the last 4.4 Gyr ³ the bright cluster galaxies did not accrete a significant mass fraction and that (dissipation-less) merging did not play a major role (see also Nelson et al. 2001).

7. Implications for the Optical and Near-Infrared Color Gradients

The role played by the Sersic index in the relation between NIR and optical structural properties (§ 6.1) suggests to discuss the combined behavior of half-light radii and Sersic indices in terms of internal color gradients.

 $^{^3\}Omega_M{=}0.3,\,\Omega_{\Lambda}=0,\,H_0=50~{\rm km~s^{-1}Mpc^{-1}}$

The available measurements of optical-NIR color gradients at intermediate redshifts concern 6 field early-type galaxies studied in V-H by Hinkley & Im (2001). Unfortunately, no one of the galaxies is close enough in z to our sample to allow a significant comparison. The comparison of recent measurements of optical color gradients at intermediate-redshifts with those in nearby galaxies shows little or no evolution since $z \sim 1$, supporting the interpretation in terms of metallicity gradients (Peletier et al. 1990b,a; Saglia et al. 2000; Tamura & Ohta 2000).

We define the color gradient as $\Delta(\mu_2 - \mu_1)/\Delta(\log r)$, where μ_i is the surface brightness in the band i, and the differences are computed between an inner (r_m) and an outer (r_M) radius. If the galaxy surface brightness in the waveband j is described by the Sersic law

$$\mu_j(r) = \mu_{0,j} + 1.086 \cdot b_j (r/r_{e,j})^{1/n_j} , \qquad (3)$$

we obtain

$$\Delta(\mu_2 - \mu_1)/\Delta(\log r) = 2.5 \log(e) \cdot \left[\log(r_M) - \log(r_m)\right]^{-1} \cdot \left[b_1 \cdot \left((r_m/r_{e,1})^{1/n_1} - (r_M/r_{e,1})^{1/n_1} \right) + b_2 \cdot \left((r_M/r_{e,2})^{1/n_2} - (r_m/r_{e,2})^{1/n_2} \right)\right],$$
(4)

where b is a function of n ($b \sim 2n - 1/3$, see Caon, Capaccioli, & D'Onofrio 1993) and the indices 1,2 denote the two wavebands. In order to make a direct comparison with previous works (Peletier et al. 1990b; Saglia et al. 2000) we set $r_m = 0.1 \cdot r_{e,R}$ and $r_M = r_{e,R}$. Equation 4 is more suitable for the present analysis than the approximation of Sparks & Jørgensen (1993), in that it allows to address the case of different values of n and it is exact for arbitrary ratios of the half-light radii. We also verified that this formula gives a very close approximation to the linear fit to the color profiles.

The V-, R- and K-band structural parameters derived in the previous sections were substituted in equation 4 to derive the implied color gradients. The uncertainties on the gradients were derived from propagation of the errors on r_e and n, taking into account the covariance term. The V-R and R-K color gradients derived by means of equation 4 are shown in Figure 11 as a function of n, and the relative median values are given in Table 7. The average optical (V-R) color gradient is $-0.06^{+0.03}_{-0.15}$ mag/dex, in agreement with the V-I gradients derived by Tamura & Ohta (2000) at z=0.37 and with the optical (V,R,I) gradients by Saglia et al. (2000) at $z\sim0.38$ for cluster early-type galaxies (see Figure 6 in Saglia et al. (2000) and Tables 2 and 3 in Tamura & Ohta 2000).

The V-R gradients present a weak trend with n: galaxies with n < 4 have larger negative gradients, with an average of -0.19 mag/dex, while for n > 4 the average gradient is consistent with zero or slightly positive (+0.07 mag/dex). The wide majority of the galaxies have negative R-K color gradients: the median value for the whole sample is $-0.49^{-0.43}_{-0.55}$

mag/dex. The trend with n is in this case stronger: the average R-K color gradient is -0.73 mag/dex for n < 4 and -0.35 mag/dex for n > 4. Furthermore, the results of § 6.1 indicate that the color gradients are mainly due to the difference in n for n < 4 and to the difference in r_e for n > 4. The optical-NIR color gradients are thus related to the relevance of the disk component, as it is apparent from Figure 11: galaxies with lower bulge-to-disk ratio $(n \to 1)$ have large R-K color gradients, while bulge-dominated galaxies have moderate gradients.

In order to probe the origin of color gradients with the large wavelength baseline provided by the K-band, we adopted two different models in which color gradients are driven by (A) 'pure age' or (M) 'pure metallicity' gradients. We used synthetic colors from the code of Bruzual & Charlot (1993) to simulate early-type galaxy spectra. An exponential star formation rate with time scale of 1 Gyr was adopted. In model (A) we assumed that the inner stellar population ($r \sim r_m$) is 6.25 Gyr old at z = 0.31. This value corresponds to the mean luminosity-weighted age of stellar populations in AC 118 galaxies as inferred from the color – magnitude relation (see Merluzzi et al. 2001). The stellar population age at the outer radius ($r \sim r_M$) was adjusted to match the observed color gradients, and the metallicity was fixed to $Z = Z_{\odot}$. In model (M) the inner stellar population is characterized by a metallicity $Z = 1.8 Z_{\odot}$ (Tamura et al. 2000) and the observed color gradients were used to derive the outer Z value. Age was fixed to 6.25 Gyr. From the median values of the R - K color gradients we derived the outer age and metallicity (τ_M and Z_M) for models (A) and (M) respectively. Such values were then used to predict the V - R color gradients at z = 0.31 and the V - R and R - K gradients at $z \sim 0$.

Table 8 gives the predicted V-R and R-K gradients along with the gradients observed both at $z \sim 0.3$ and at $z \sim 0$. Optical-NIR color gradients were measured for 12 nearby bright elliptical galaxies by Peletier et al. (1990a, b). From their data we obtain an average R-K gradient of -0.14, with a broad distribution of values ranging from -0.62 to +0.15. Pahre et al. (1998) estimated an average V-K gradient of -0.18 by applying the formula of Sparks & Jørgensen (1993) to the ratio of the relative half-light radii, while an average V-H gradient of ~ -0.18 can be inferred in the same way from the Coma cluster H and V effective radii given by Scodeggio et al. (1998).

The results shown in Table 8 may be summarized as follows. The pure age model is able to explain the evolution of the R-K color gradient between $z\sim 0.3$ and $z\sim 0$, but it fails to describe the V-R gradient at $z\sim 0.3$. Conversely, the pure metallicity model is able to reconcile the V-R and R-K color gradients at $z\sim 0.3$, but it fails to describe the evolution of the R-K gradient as a function of look-back time.

8. Discussion and Conclusions

In this study we derived optical and NIR structural parameters for galaxies belonging to the cluster AC 118 at z=0.31 from ground-based photometry. The present data set constitutes the first large sample of structural parameters determined at intermediate redshifts in different wavebands and, in particular, it is the first such sample in the near-infrared. The samples consist in N=93 objects studied in the R and K wavebands and in N=58 galaxies studied in the V-band.

The reliability of the data was verified by comparison with the results from HST photometry for a subsample of galaxies: the scatter between measurements from HST- and from ground-based photometry is equivalent to the scatter between parameters determined with two different fitting methods from HST images, namely of $\sim 35\%$ in r_e . Given that these values of the scatter are generally claimed to be a measure of the 'intrinsic uncertainty' in structural parameter measurements, we can state that reliable structural parameters can be still derived from ground-based photometry in ordinary observing conditions at least up to $z \sim 0.3$.

Since morphology was not a selection criterion in this study, some remarks are needed for the comparison of our results with other works. Couch et al. (1998) established that 78% of the galaxies in the core of AC 118 are early-types while 22% are spirals. They also found a significant rise in the fraction of S0 galaxies with respect to the local density-morphology relation. Morphological classification from Couch et al. (1998) is available for 21 galaxies in sample D. The number of spirals is 5, of which 3 have n < 1.5 while the other two have $n \gtrsim 4$. Only one of the spirals has 'late-type' colors, while the others lie on the red sequence of AC 118. It is interesting to notice that all the remaining galaxies with 'late-type' colors lie outside of the cluster core and have n < 2. They are likely disk galaxies dominated by young stellar populations. These facts are in agreement with a scenario in which spirals are accreted into the cluster from the field, cease to form stars, become gas-deficient objects and eventually undergo a morphological transformation (Couch et al. 1998). The remaining galaxies with morphological information consist in 10 S0, eight of which with $2 \lesssim n \lesssim 3$ and two with $n \sim 8$, and 6 ellipticals, for which we find $n \gtrsim 4$. We stress that the galaxies with large disks and late-type colors are only 4% of galaxies in sample D.

The main feature concerning the multi-band properties of galaxies is that these are much more concentrated in the NIR than in the optical. The mean ratio of NIR to optical half-light radii (~ 0.75) is not different from that found in local samples of early-type galaxies (~ 0.8 , e.g. Pahre 1999), but the situation is complicated by the systematic differences found in the shape of the brightness distribution: galaxies with low n value have a light profile more peaked in the center in the K-band ($n_K - n_R \sim 1$), while for $n \gtrsim 4$ a lower $r_{e,K}/r_{e,R}$ is

observed (~ 0.6). Such trends can be interpreted as due to the increase of the disk fraction when n approaches unity.

To discuss the combined effects of half-light radii and Sersic indices, we derived the optical and NIR color gradients by means of equation 4. Most of galaxies in AC 118 do not show significant optical color gradients, with a median value of $-0.06^{+0.03}_{-0.15}$. This result is consistent with previous estimates of optical color gradients at intermediate redshifts (Saglia et al. 2000; Tamura & Ohta 2000). Conversely, strong negative gradients are found in optical–NIR colors: the median of the R-K gradients amounts to $-0.49^{-0.43}_{-0.55}$. Moreover, this effect depends on the shape of the light profile: the R-K gradient increases from $-0.73^{-0.63}_{-0.83}$ for galaxies with low n value to $-0.35^{-0.29}_{-0.42}$ for $n \gtrsim 4$. Again this result can be explained by an increase in the disk fraction when $n \to 1$.

To interpret these results in terms of the properties of the stellar populations, we introduced a pure age and a pure metallicity model. We used the R-K gradients to calibrate both models and to predict V-R color gradients at z=0.31. Moreover, the evolution of color gradients as inferred by the models was compared with the measurements by Peletier et al. (1990a,b) for a sample of nearby elliptical galaxies. The age model is not able to reconcile our optical and NIR estimates at z=0.31 since a significant negative gradient is predicted in V-R (~ -0.26). On the other hand, the predicted color gradient agree with the measurements at z=0. Conversely, the pure metallicity model gives correct results at z=0.31 but predicts too strong NIR gradients at z=0. Since the age model is able to describe the evolution of color gradients, whereas the metallicity model correctly explains the dependence of color gradients on wavelength, we argue that a model in which effects of age and metallicity are consistently combined could explain optical and NIR color gradients from z = 0.31 up to z = 0. Finally, we remark that dust likely affects the optical-NIR color gradients. Dust is actually presents in the core of most early-type galaxies (Goudfrooji & de Jong 1995; van Dokkum & Franx 1996) and is known to produce high central color gradients in bulges of S0 and spiral galaxies (e.g. Peletier et al. 1999).

The distributions of both the optical and NIR half-light radii of galaxies at $z\sim0.3$ are found to be consistent with those of Coma early-type galaxies. The result for the NIR waveband is the most significant, since the NIR probes directly the mass distribution inside galaxies. The observed distributions thus indicate that the sizes of bright galaxies did not substantially change since $z\sim0.3$ to the present epoch. This result suggests that (dissipation-less) merging did not play a major role in galaxy evolution during the last 4.4 Gyr (see also Nelson et al. 2001).

We are grateful to Adam Stanford who provided us with his own photometry of AC 118,

that was used to check the calibration of our R-band data. We thank the referee for his/her helpful comments and suggestions and Dr. M. D'Onofrio helpful discussions. The observations at ESO were collected during the guaranteed time of the Osservatorio Astronomico di Capodimonte. This work is partially based on observations made with the NASA/ESA Hubble Space Telescope, obtained from the data archive at the Space Telescope Science Institute. STScI is operated by the Association of Universities for Research in Astronomy, Inc. under NASA contract NAS 5-26555. Michele Massarotti is partly supported by a MURST-COFIN grant.

A. Calibration of HST data

AC 118 was observed on November 1994 with the HST Wide-Field Planetary Camera 2 in the F702W filter. Two exposures of 2300 s and one exposure of 1900 s for a total integration time of 6500 s are available for a single pointing.

The HST images were calibrated into the Johnson R-band by means of the NTT photometry. We proceeded as follows. The frames were smoothed to the same resolution of ground-based images by a convolution with the NTT R-band PSF. Aperture photometry was then performed with the SExtractor software (Bertin & Arnouts 1996) in the same aperture of the ground data. Figure 12 shows the difference of R and F702W instrumental magnitudes versus V-R colors. The data points were fitted with the equation:

$$R = F702W_{instr} + a * (V - R) + b .$$

We found $a = 30.93 \pm 0.10$ and $b = 0.30 \pm 0.12$, and that the root mean square of the residuals to the fitted relation varies from 0.05 mag for $R \le 20.5$ mag to 0.1 mag for the whole sample. The few galaxies (9%) which deviate more than ~ 0.2 mag from the fit, turned out to be objects contaminated by bright neighbors. In the same figure we also plot the synthetic transformation to the R waveband of Holtzman et al. (1995, see their equation 9 and Table 10):

$$R = F702W_{instr} + 0.486 * (V - R) - 0.079 * (V - R)^{2} + + 2.5 * log(t_{exp}) + 2.5 * log(GR) + \Delta m_{ap} + \Delta m_{exp} ,$$
(A1)

where t_{exp} is the exposure time, GR is the gain ratio of the WFPC2 chips, Δm_{ap} is an aperture correction term derived from the encircled energy measurements of Holtzman et al. (1995), and Δm_{exp} is the long exposure correction term from Hill et al. (1998). The same gain ratio GR = 2 was adopted for each chip, since the effects of gain differences are very small ($\lesssim 0.01$ mag) when compared to the other sources of uncertainty. We adopted $\Delta m_{ap} = +0.10$ mag and $\Delta m_{exp} = +0.05$ mag. A further shift of +0.05 mag was needed to better match equation A1 to our data. This is in agreement with previous results of calibration of HST images with ground-based photometry (see Jørgensen et al. 1999).

B. PSF of ground-based images

The PSF of NTT ground-based images was described by the following model:

$$S(x,y) = [G_1 + G_2] *R(x,y) ,$$
(B1)

where S is the PSF brightness distribution, $G_j(j=1,2)$ are two-dimensional Gaussian functions and R is a box function equal to 1 on the pixel area and 0 elsewhere. The convolution in equation B1 was computed from the one-dimensional convolution of a Gaussian with a rectangular function. For the one-dimensional case, the following expression is obtained:

$$g*r(x) = (2a)^{-1} \cdot \left\{ Erf\left[\frac{a/2+x}{\sqrt{2}\sigma}\right] + Erf\left[\frac{a/2-x}{\sqrt{2}\sigma}\right] \right\} ,$$
 (B2)

where g(x) is a normal Gaussian function of width parameter σ , r(x) is a rectangle of width a, and Erf(x) is the error function. The analytical expression of the ground-based PSF is obtained by substituting the formula B2 in equation B1.

C. Uncertainties on galaxy structural parameters

Galaxy structural parameters were derived by minimizing the right side of equation 2, i.e. by solving the following system of equations:

$$\frac{\partial}{\partial p_k} \chi^2(\{p_k\}; \{I_j\}, \{s_l\}) = 0 \quad , \tag{C1}$$

where χ^2 is a function of the fitting parameters $\{p_k\}$, $\{I_j\}$ are the brightness values of image pixels, and $\{s_l\}$ are the PSF parameters for the ground-based data. The changes $\{\delta I_j\}$, $\{\delta s_l\}$ of $\{I_j\}$ and $\{s_l\}$ determine variations $\{\delta \bar{p}_k\}$ of the solutions $\{\bar{p}_k\}$ of equations C1. At the first order, $\{\delta \bar{p}_k\}$ are obtained from the following formulae:

$$\delta \bar{p} = H^{-1} \cdot (A \cdot \delta I + B \cdot \delta s) \quad , \tag{C2}$$

where the symbol \cdot denotes matrix multiplication, $\delta \bar{p}$, δI and δs are column vectors of components $\delta \bar{p}_k$, δI_j and δs_l respectively, H^{-1} is the inverse of the χ^2 Hessian matrix, A and B are rectangular matrices of components $\partial \chi^2/\partial p_k \partial s_l$ and $\partial \chi^2/\partial p_k \partial I_j$ respectively. All quantities are computed at $\{\bar{p}_k\}$, $\{I_j\}$ and $\{s_l\}$.

The noise of image pixels and the uncertainties on PSF parameters (see § 3.1) were used to estimate the quantities $\{\delta I_j\}$ and $\{\delta s_l\}$. Uncertainties on fitting parameters were then derived by equations C2.

REFERENCES

Allen, S.W. 2000, MNRAS, 315, 269

Andreon, S. 2001, ApJ, 547, 623

Barger, A.J., Aragón-Salamaca, A., Ellis, R.S., Couch, W.J., Smail, I., & Sharples, R.M. 1996, MNRAS, 279, 1

Bertin, E., Arnouts, S. 1996, A&AS, 117, 393

Bower, R.G., Lucey, J.R., & Ellis, R.S. 1992, MNRAS, 254, 601

Bruzual, G.A., & Charlot, S. 1993, ApJ, 405, 538

Caon, N., Capaccioli, M., & D'Onofrio, M. 1993, MNRAS, 265, 1013

Capaccioli, M., Caon, N., & D'Onofrio, M. 1992, MNRAS, 259, 323

Couch, W.J., Barger, A. J., Smail, I., Ellis, R. S., & Sharples, R. M. 1998, ApJ, 497, 188

Djorgovski, S., & Davies, M. 1987, ApJ, 313, 59

Dresseler, A., Lynden-Bell, D., Burstein, D., Davies, R.L., Faber, S.M., Terlevich, R.J., & Wegner, G. 1987, ApJ, 313, 42

Goudfrooij, P., & de Jong, T. 1995, A&A, 298, 784

Govoni, F., Enßlin. T.A., Feretti, L., & Giovannini, G. 2001, A&A, 369, 441

Hamabe, M., & Kormendy, J. 1987, IAU Symp. No. 127, ed. T. de Zeeuw, Dordreech: Reidel, 379

Hill, R. J. 1998, ApJ, 496, 648

Hinkley S., & Im, M. 2001, ApJ, 560, L41

Holtzman, J. A. et al. 1995, PASP, 107, 156

Jørgensen, I., Franx, M., & Kjærgaard, P. 1995, MNRAS, 273, 1097

Jørgensen, I., Franx, M., & Kjærgaard, P. 1996, MNRAS, 280, 167

Jørgensen, I., Franx, M., Hjorth, J., & van Dokkum, P. G. 1999, MNRAS, 308, 833

Kauffmann, G., & Charlot, S. 1998, MNRAS, 294, 705

Kelson, D.D., Illingworth, G.D., van Dokkum, P.G., & Franx, M. 2000a, ApJ, 531, 184

Kelson, D.D., Illingworth, G.D., van Dokkum, P.G., & Franx, M. 2000b, ApJ, 531, 137

Kodama, T., & Arimoto, N. 1997, A&A, 320, 41

Kodama, T., Arimoto, N., Barger, A.J, & Aragón-Salamanca, A. 1998, A&A, 334, 99

Kormendy, J. 1977, ApJ, 218, 333

Krist, J. 1999, "The Tiny Tim User's Guide", version 5.0, STScI, Baltimore

Lubin, L. M., & Sandage, A. 2001, AJ, 121, 2289

Massarotti, M., Iovino, A., & Buzzoni, A. 2001, A&A, 368, 74

Merluzzi, P., Busarello, G., Massarotti, M., & La Barbera, F. 2001, in ASP Conf. Ser., in press (astro-ph/0110328)

Nelson, A.E., Simard, L., Zaritsky, D., Dalcanton, J.J., & Gonzalez, A.H. 2001, preprint (astro-ph/0110582)

Pahre, A.M., de Carvalho, R.R., & Djorgovski, S.G. 1998, AJ, 116, 1606

Pahre, M.A. 1999, ApJS, 124, 127

Peletier, R.F., Davies, R.L., Davies, L.E., Illingworth, G.D., & Cawson, M. 1990a, AJ, 100, 1091

Peletier, R.F., Valentijn, E.A., & Jameson, R.F. 1990b, A&A, 233, 62

Peletier, R.F., Vazdekis, A., Arribas, S., del Burgo, C., García-Lorenzo, B., Gutiérrez, C., Mediavilla, E., & Prada, F. 1999, MNRAS, 310, 863

Press, W.H., Flannery, B.P., Teukolsky, S.A., & Vetterling, W.T. 1986, Numerical Recipes (Cambridge: Cambridge Univ. Press)

Ratnatunga, K.U., Griffiths, R.E., & Ostrander, E.J. 1999, AJ, 118, 86

Saglia, R.P., Bertschinger, E., Baggley, G., Burstein, D., Colless, M., Roger, L.D., McMahan, R.K., Jr., & Wegner, G. 1997, ApJS, 109, 79

Saglia, R.P., Maraston, C., Greggio, L., Bender, R., & Ziegler, B. 2000, A&A, 360, 911

Schade, D., Lilly, S.J., Le Fevre, O., Hammer, F., & Crampton, D. 1996, ApJ, 464, 79

Scodeggio, M., Gavazzi, G., Belsole, E., Pierini, D., & Boselli, A. 1998, MNRAS, 301, 1001

Scodeggio, M. 2001, AJ, 121, 2413S

Sersic, J.L. 1968, Atlas de Galaxias Australes, Observatorio Astronomico, Cordoba

Simard, L., Koo, D.C., Faber, S.M., Sarajedini, V.L., Vogt, N.P., Phillips, A.C., Gebhardt, K., Illingworth, G.D., & Wu, K.L. 1999, ApJ, 519,563

Smith, R.J., Lucey, J.R., Hudson, M.J., & Steel, J. 1997, MNRAS, 291, 461

Sparks, W.B., & Jørgensen, I. 1993, AJ, 105, 1753

Stanford, S.A., Eisenhardt, P.R.M., & Dickinson, M. 1998, ApJ, 492, 461

Tamura, N., Kobayashi, C., Arimoto, N., Kodama, T., & Ohta, K. 2000, MNRAS, 119, 2134

Tamura, N., & Ohta, K. 2000, AJ, 120, 533

van Dokkum, P.G., & Franx, M. 1996, MNRAS, 281, 985

van Dokkum, P.G., & Franx, M. 2001, ApJ, 553, 90

Williams, L.L.R., Navarro, J.F., & Bartelmann M. 1999, ApJ, 527, 535

Wu, X-P., Xue, Y-J., & Fang L-Z. 1999, ApJ, 524, 22

Ziegler, B.L., & Bender, R. 1997, MNRAS, 291, 527

Ziegler, B.L., Saglia, R.P., Bender, R., Belloni, P., Greggio, L., & Seitz, S. 1999, A&A, 346, 13

This preprint was prepared with the AAS IATEX macros v5.0.

- Fig. 1.— Dependence of the ground-based PSF on the chip position. The quantities shown in the figure are: the ratio of the central intensities of the 'outer' and 'inner' Gaussians I_2/I_1 , the FWHM in the x- and y- directions of the inner Gaussian $(FWHM_x^{(1)})$ and $FWHM_y^{(1)})$, the FWHM in the x- and y- directions of the outer Gaussian $(FWHM_x^{(2)})$ and $FWHM_y^{(2)}$, and the asymmetry $A = FWHM_x^{(1)}/FWHM_y^{(1)}$ of the inner Gaussian. On the x-axis the distance to the frame centers d is plotted. For each quantity, three panels are shown for the V-, R- and K-bands as indicated in the upper-left plots. The error bars correspond to 1σ standard intervals and the solid lines are the curves used to create the PSF models for each galaxy position (see text).
- Fig. 2.— Results of the numerical simulations for R-band photometry. The differences between input and output values are shown for the following quantities: logarithm of r_e , $\langle \mu \rangle_e$, m_T , fundamental plane parameter FP, logarithm of the axis ratio b/a, and n. For each quantity, the two panels correspond to simulations with $r_e = 0.3''$ and $r_e = 0.6''$. The total magnitude of the models is given on the abscissae.
- Fig. 3.— Minimum r_e for the applicability of the 2-D fitting to the ground-based data. The same quantities as in Figure 2 are plotted on the vertical axis while the logarithm of the 'true' effective radius is shown on the abscissae. For each quantity, the three panels correspond to the different values of n (see upper-left panels).
- Fig. 4.— Two-dimensional fit of galaxies in the HST image by means of Sersic and of B+D models. Left and right pictures are relative to galaxies with F=+1 and F=0 (see text). Upper panels: original image; middle left and right panels: Sersic and B+D fitting models; lower panels: corresponding residuals.
- Fig. 5.— Distribution of the differences between structural parameters derived from the Sersic fit and from the B+D decomposition for HST galaxies. From left to right, and from top to bottom: r_e , $\langle \mu \rangle_e$, m_T and FP parameter. Solid, dashed and dot-dashed lines are relative to galaxies with different fitting flag F as indicated in the upper-left panel. Differences are in the direction Sersic-(B+D).
- Fig. 6.— Two-dimensional fit of galaxies in the HST F702W and NTT R-band images. For each quadrant, the left and right panels correspond to NTT and HST data respectively, and, from top to bottom, galaxy image, fitting model, and image of residuals are shown. HST and NTT images are scaled to the same counts/arcsec².

Fig. 7.— Comparison of structural parameters derived from NTT R and HST F702W images. For each panel, the histograms show the fractional distribution of differences between NTT and HST parameters. The plotted quantities and the plotting ranges are the same as in Figure 5. Differences are in the direction NTT – HST.

Fig. 8.— Differences (V - R) of structural parameters derived from V and R images. The R-band n is plotted on the abscissae.

Fig. 9.— Distribution of optical (upper panel) and NIR (bottom) half-light radii of: 1) cluster galaxies at z=0.31 (solid line, this work); 2) cluster galaxies at z=0.33 (dashed line, Kelson et al. 2000b); early-type galaxies in Coma (z=0.023, dash-dotted line, Pahre 1999). The Coma radii were transformed to z=0.31 by adopting $\Omega_M=0.3$ and $\Omega_{\Lambda}=0$.

Fig. 10.— Differences (K - R) of structural parameters derived from R and K images. The R-band n is plotted in the abscissae. The plotting ranges are the same as in Figure 8.

Fig. 11.— Color gradients of AC 118 galaxies as derived from equation 4 (see text). V-R and R-K color gradients are shown in the upper and lower panel respectively. The Sersic index in the R-band is plotted on the abscissae. Error bars define 1σ standard intervals.

Fig. 12.— Calibration of HST data by ground-based NTT photometry. Differences of R and F702W instrumental magnitudes are plotted versus V-R. The solid line is the least squares fit to the data. The dashed curve represents the synthetic transformation of Holtzman et al. (1995).

Table 1. Summary of the photometric data.

Band	Instrument	Exp. Time (sec)	Field	pixel scale (arcsec/pxl)	seeing (arcsec)
V	NTT-EMMI	2700	9.′15×8.′6	0.267	1.2
\mathbf{R}	"	1800	"	"	1.0
$ m K \\ F702W$	NTT-SOFI HST-WFPC2	15900 6500	$5' \times 5'$ $5.8 \mathrm{arcmin}^2$	$0.292 \\ 0.1$	0.8

 ${\bf Table\ 2.}\quad {\bf Description\ of\ the\ samples.}$

	A	В	C	D
wavebands	F702W	R, F702W	V,R	R,K
phot. redshift	all	all	0.3	0.3
selection	$R \le 21, r_e > 0.15''$	$R \le 21, r_e > 0.15''$	$R \le 21, V \le 20.5, r_e > 0.15''$	$R \le 21, r_e > 0.15''$
N	50	37	58	93
fitting models	$B+D, r^{1/n}$	$r^{1/n}$	$r^{1/n}$	$r^{1/n}$

Table 3. Comparison of Sersic and B + D fitting parameters.

F	$\Delta \log$	r_e	$\Delta\langle\mu angle$	e	 Δm	Γ	 ΔF	P
	m	std	m	std	m	std	m	std
-1	$-0.06^{+0.09}_{-0.19}$	$0.32_{0.29}^{0.47}$	$0.40^{+0.24}_{-0.90}$	$1.3_{1.2}^{1.8}$	$-0.10^{+0.26}_{-0.23}$	$0.43_{0.37}^{0.95}$	$+0.06^{+0.10}_{+0.00}$	$0.10^{0.14}_{0.09}$
0	$0.002^{+0.024}_{-0.031}$	$0.13_{0.12}^{0.16}$	$0.03^{+0.14}_{-0.10}$	$0.56_{0.50}^{0.68}$	$0.04^{+0.07}_{-0.001}$	$0.17^{0.21}_{0.15}$	$-0.011^{+0.001}_{-0.021}$	$0.047^{0.057}_{0.042}$
1	$-0.06^{+0.003}_{-0.11}$	$0.20^{0.30}_{0.17}$	$-0.20^{+0.07}_{-0.40}$	$0.79^{1.20}_{0.66}$	$0.12^{+0.18}_{+0.04}$	$0.24_{0.21}^{0.34}$	$-0.003^{+0.005}_{-0.02}$	$0.036_{0.030}^{0.060}$
-1,0,1	$-0.03^{+0.001}_{-0.056}$	$0.185_{0.17}^{0.22}$	$-0.10^{+0.016}_{-0.21}$	$0.76_{0.70}^{0.87}$	$0.04^{+0.08}_{+0.006}$	$0.24_{0.22}^{0.28}$	$0.001^{+0.010}_{-0.007}$	$0.06_{0.05}^{0.07}$

Note. — Column 1: fitting flag F. Columns 2, 3, 4 and 5: medians and standard deviations of the differences of the structural parameters. The upper and lower values define the 68% confidence interval. Differences are in the direction Sersic - (B+D).

Table 4. Comparison of HST and NTT R-band fitting parameters.

		, 7
	m	std
$\Delta(\log r_e)$	$-0.04^{+0.002}_{-0.08}$	$0.16^{0.21}_{0.14}$
$\Delta(\langle\mu\rangle_e)$	$-0.15_{-0.26}^{-0.04}$	$0.67_{0.60}^{0.80}$
$\Delta(m_T)$	$-0.08^{-0.03}_{-0.12}$	$0.30_{0.28}^{0.33}$
$\Delta(FP)$	$+0.020^{+0.037}_{+0.004}$	$0.06_{0.05}^{0.08}$
$\Delta(\log b/a)$	$+0.011^{+0.024}_{+0.003}$	$0.082^{0.095}_{0.075}$
$\Delta(n)$	$+0.01^{+0.45}_{-0.40}$	$2.6^{2.9}_{2.4}$
	0.10	

Note. — Median and standard deviation of quantities in column 1 are shown in columns 2 and 3. Upper and lower values define the 68% confidence interval. Differences are in the direction NTT-HST.

Table 5. Comparison of NTT V- and R-band structural parameters.

		. 7
	m	std
$\Delta(\log r_e)$	$+0.014^{+0.04}_{-0.004}$	$0.17_{0.14}^{0.26}$
$\Delta(\langle\mu\rangle_e)$	$+0.019^{+0.12}_{-0.07}$	$0.75_{0.63}^{1.00}$
$\Delta(m_T)$	$-0.045^{-0.016}_{-0.083}$	$0.26_{0.22}^{0.34}$
$\Delta(FP)$	$+0.008^{+0.020}_{-0.001}$	$0.08_{0.07}^{0.09}$
$\Delta(\log b/a)$	$-0.010^{-0.002}_{-0.017}$	$0.06_{0.05}^{0.07}$
$\Delta(n)$	$+0.024^{+0.27}_{-0.21}$	$1.9_{1.8}^{2.2}$

Note. — See Table 4. Differences are in the direction V-R.

Table 6. Comparison of NTT K- and R-band structural parameters.

	all	l $n < l$		4	n > 4	1
	m	std	m	std	m	std
$\Delta(\log r_e)$	$-0.125^{-0.11}_{-0.14}$	$0.19_{0.18}^{0.21}$	$-0.09^{-0.07}_{-0.11}$	$0.12^{0.14}_{0.11}$	$-0.20^{-0.17}_{-0.24}$	$0.23_{0.21}^{0.26}$
$\Delta(\langle\mu\rangle_e)$	$-0.56_{-0.63}^{-0.47}$	$0.94_{0.89}^{1.02}$	$-0.37^{-0.29}_{-0.46}$	$0.68_{0.60}^{0.81}$	$-0.78_{-0.93}^{-0.66}$	$1.12_{1.05}^{1.23}$
$\Delta(m_T)$	$+0.04^{+0.09}_{-0.01}$	$0.26_{0.25}^{0.29}$	$-0.04_{-0.10}^{-0.02}$	$0.18^{0.22}_{0.16}$	$+0.15_{+0.08}^{+0.23}$	$0.29_{0.27}^{0.33}$
$\Delta(FP)$	$+0.04^{+0.05}_{+0.01}$	$0.11_{0.10}^{0.12}$	$+0.04^{+0.06}_{+0.015}$	$0.09_{0.08}^{0.11}$	$+0.035^{+0.053}_{+0.015}$	$0.13_{0.12}^{0.14}$
$\Delta(\log b/a)$	$-0.002^{+0.005}_{-0.009}$	$0.060_{0.055}^{0.067}$	$-0.005^{+0.007}_{-0.014}$	$0.060_{0.056}^{0.067}$	$+0.000^{+0.007}_{-0.008}$	$0.60^{0.76}_{0.52}$
$\Delta(n)$	$+0.52^{+0.60}_{+0.48}$	$2.0_{1.9}^{2.2}$	$+0.95^{+1.0}_{+0.85}$	$1.6_{1.5}^{1.9}$	$+0.08^{+0.15}_{+0.02}$	$2.2_{2.0}^{2.5}$

Note. — Medians and standard deviations are shown for galaxies with different ranges of n. Differences are in the direction K - R.

Table 7. Median values of V-R and R-K color gradients of AC 118 galaxies.

	all	n < 4	n > 4
(V - R) $(R - K)$	$-0.06^{+0.03}_{-0.15}$ $-0.49^{-0.43}_{-0.55}$	$-0.19_{-0.28}^{-0.09}$ $-0.73_{-0.83}^{-0.63}$	$+0.07^{+0.18}_{-0.04}$ $-0.35^{-0.29}_{-0.42}$

Note. — Color gradients are in units of mag/dex.

Table 8. Computed and observed color gradients.

MODEL	$grad(V-R)$ $z\sim0.3$	$ grad(V - R) $ $ z \sim 0 $	$grad(R-K)$ $z\sim0.3$	$ grad(R-K) $ $ z \sim 0 $
$\begin{array}{c} \text{AGE} \\ \tau_M = 3.2 Gyr \end{array}$	-0.26	-0.04	-0.49^{a}	-0.13
$METALLICITY$ $Z_M = 0.5 Z_{\odot}$	-0.15	-0.10	-0.49 ^a	-0.41
observed	-0.1 ^b	-0.02^{c}	-0.49^{d}	-0.14^{c}

^a Constrain to the model.

Note. — The predictions are based on pure age and pure metallicity gradient models (see text). Column 1: adopted model. Column 2, 3: optical – optical color gradient at $z\sim0.3$ and $z\sim0$ respectively. Column 4: optical – NIR color gradient at z=0. color gradients are reported in units of mag/dex.

 $^{^{\}rm b}$ See Tamura & Ohta (2000); Tamura et al. (2000); Saglia et al. (2000), and this work.

^c See Peletier et al. (1990a, b).

^d This work.

This figure "f1.gif" is available in "gif" format from:

This figure "f2.gif" is available in "gif" format from:

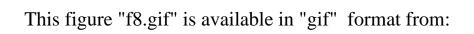
This figure "f3.gif" is available in "gif" format from:

This figure "f4.gif" is available in "gif" format from:

This figure "f5.gif" is available in "gif" format from:



This figure "f7.gif" is available in "gif" format from:



This figure "f9.gif" is available in "gif" format from:

This figure "f10.gif" is available in "gif" format from:

This figure "f11.gif" is available in "gif" format from:

This figure "f12.gif" is available in "gif" format from: